

Published in final edited form as:

J Inorg Biochem. 2011 April ; 105(4): 509–517. doi:10.1016/j.jinorgbio.2010.12.012.

Rational Design, Synthesis and Evaluation of First Generation Inhibitors of the *Giardia lamblia* Fructose-1,6-biphosphate Aldolase

Zhimin Li¹, Zhengang Liu, Dae Won Cho¹, Jiwen Zou¹, Maozhen Gong¹, Robert M. Breece², Andrey Galkin³, Ling Li¹, Hong Zhao¹, Gabriel D. Maestas¹, David L. Tierney², Osnat Herzberg³, Debra Dunaway-Mariano^{1,*}, and Patrick S. Mariano^{1,*,+}

¹Department of Chemistry and Chemical Biology, University of New Mexico, Albuquerque, New Mexico 87131

²Department of Chemistry and Biochemistry, Miami University, Oxford, Ohio 45056

³Center for Advanced Research in Biotechnology, University of Maryland Biotechnology Institute, Rockville, Maryland 20850

Abstract

Inhibitors of the *Giardia lamblia* fructose 1,6-bisphosphate aldolase (*G/FBPA*), which transforms fructose 1,6-bisphosphate (FBP) to dihydroxyacetone phosphate and glyceraldehyde 3-phosphate, were designed based on 3-hydroxy-2-pyridone and 1,2-dihydropyridine scaffolds that position two negatively charged tetrahedral groups for interaction with substrate phosphate binding residues, a hydrogen bond donor to the catalytic Asp83, and a Zn²⁺ binding group. The inhibition activities for the *G/FBPA* catalyzed reaction of FBP of the prepared alkyl phosphonate/phosphate substituted 3-hydroxy-2-pyridinones and a dihydropyridine were determined. The 3-hydroxy-2-pyridone inhibitor **8** was found to bind to *G/FBPA* with an affinity (K_i = 14 μM) that is comparable to that of FBP (K_m = 2 μM) or its inert analog TBP (K_i = 1 μM). The X-ray structure of the *G/FBPA*-inhibitor **8** complex (2.3 Å) shows that **8** binds to the active site in the manner predicted by *in silico* docking with the exception of coordination with Zn²⁺. The observed distances and orientation of the pyridone ring O=C-C-OH relative to Zn²⁺ are not consistent with a strong interaction. To determine if Zn²⁺ coordination occurs in the *G/FBPA*-inhibitor **8** complex in solution, EXAFS spectra were measured. A four coordinate geometry comprised of the three enzyme histidine ligands and an oxygen atom from the pyridone ring O=C-C-OH was indicated. Analysis of the Zn²⁺ coordination geometries in recently reported structures of class II FBPAs suggests that strong Zn²⁺ coordination is reserved for the enediolate-like transition state, accounting for minimal contribution of Zn²⁺ coordination to binding of **8** to *G/FBPA*.

Corresponding Authors: P. S. Mariano mariano@unm.edu and Debra Dunaway-Mariano dd39@unm.edu.

⁺Inhibitor synthesis was carried out by Z. L., D. W. C., J. Z., M. G. and G. D. M under the direction of P. S. M., protein preparations and kinetic studies were carried out by Z. L., L. Li and H. Z. under the direction of D.D.-M., EXAFS studies were carried out by R. M. B. under the direction of D. L.T., and the crystal structure determination was made by A. G. under the direction of O. H. The manuscript was written by P.S.M. and D.D.-M.

The atomic coordinates and structure factors have been deposited in the Protein Data Bank.

Appendix A. Supplementary Data: Experimental procedures for inhibitor syntheses and spectroscopic data for all previously unreported compounds shown in Schemes 1 and 2 are given. Best fits to raw EXAFS data for FBPA inhibitors, corresponding to those presented in Figure 5 and Table 3, are given in Figure SII.

Publisher's Disclaimer: This is a PDF file of an unedited manuscript that has been accepted for publication. As a service to our customers we are providing this early version of the manuscript. The manuscript will undergo copyediting, typesetting, and review of the resulting proof before it is published in its final citable form. Please note that during the production process errors may be discovered which could affect the content, and all legal disclaimers that apply to the journal pertain.

Keywords

Fructose-1,6-bisphosphate aldolase; inhibition; *Giardia lamblia*; Zn²⁺ coordination; hydroxypyridinone; dihydroxypyridine; EXAFS; protein structure; metal coordination; inhibitor design

1. Introduction

Giardia lamblia, a waterborne human parasite, inflicts billions of people worldwide with a chronic infection (giardiasis) that leads to malnutrition, growth retardation in children, and sometimes death [1-3]. Because of its impact on impoverished countries, and the meager effort expended to identify new therapies, giardiasis has been designated as a World Health Organization neglected disease [4]. In addition, the Center for Disease Control has classified *Giardia* as a bioterrorism category B organism. The drugs metronidazole and tinidazole, which are currently used to treat giardiasis, produce problematic side effects. Moreover, the rate of recurrence of infection is high, and the existence of resistant strains has been documented [5-8]. The cellular biology and biochemistry of *G. lamblia* are not well defined nor are its host adaptation and survival tactics. However, the *G. lamblia* genome sequence is now known [9] and, thus, understanding and controlling *G. lamblia* pathogenicity are tractable objectives.

Recent studies in our laboratories have focused on the identification, characterization and design of inhibitors of enzymes that constitute potential *G. lamblia* drug targets. From the outset, the class II fructose 1,6-bisphosphate aldolase (FBPA) was viewed as a particularly attractive target. FBPA catalyzes the reversible cleavage of D-fructose 1,6-bisphosphate (FBP) to dihydroxyacetone phosphate (DHAP) and D-glyceraldehyde 3-phosphate (G3P) (Fig. 1), a key step in the Embden-Meyerhof-Parnas glycolytic pathway. Because *G. lamblia* lacks the components of oxidative energy metabolism, the generation of ATP via the glycolytic pathway is likely to be essential for trophozoite colonization of the human gut [10-12]. This assumption gains support from the finding that RNAi/antisense RNA FBPA gene silencing in transfected *G. lamblia* trophozoites is lethal under standard culture conditions [13].

FBPA function is also essential to the human host. Nevertheless, through strategic design of mechanism-based inhibitors, it might be possible to eliminate the activity of the *G. lamblia* FBPA (*G*/FBPA) without interfering with the activity of the human FBPA. This proposal is based on the fact that the *G*/FBPA and human FBPA evolved within different protein fold families and thus possess different active site structures and, most importantly, they employ different catalytic mechanisms. *G*/FBPA is a class II aldolase [14], that uses a Zn²⁺ cofactor to activate FBP for retro-aldol cleavage [15-18] whereas the human FBPA is a class I aldolase that utilizes an active site lysine to activate cleavage of FBP via Schiff base formation [19-21] (Fig. 1). Enzymes that employ Zn²⁺ in substrate activation are susceptible to inhibition by small molecules that possess Zn²⁺-binding groups. Examples of Zn²⁺-dependent enzymes which have been successfully modulated *in vivo* with small molecule inhibitors equipped with a “Zn²⁺-warhead” include carbonic anhydrase [22], matrix metalloprotease [23] and histone deacetylase [24].

The X-ray structures of *G*/FBPA bound with substrate and substrate analogs provide the needed insight into the steric and electrostatic features of the active site that govern ligand binding. Most helpful to new inhibitor design is the 1.8 Å resolution structure of *G*/FBPA bound with the inert substrate analog tagatose 1,6-bisphosphate (TBP) (a C(4) epimer of FBP) [25]. This structure defines a solvent excluded pocket that accommodates both the

Zn²⁺ cofactor and the TBP C(1)-C(3) unit (Fig. 2A) and shows that the TBP C(4)-C(6) unit extends along the protein surface. The polar interactions observed between the TBP ligand and the binding site residues are extensive (Fig. 2B). The Zn²⁺ cofactor is bound to the enzyme through the coordination bonds formed with the imidazole rings of His84, His178 and His210 (Fig. 2B).

The design of first generation of *GIFBPA* inhibitors described below centers on a synthetically accessible scaffold that positions two highly negatively charged, tetrahedral groups for interaction with the numerous substrate C(1) and C(6) phosphate binding residues, a hydrogen bond donor to the catalytic Asp83, and a Zn²⁺ binding group (Fig. 2C). In the effort described, alkyl phosphonate/phosphate substituted 3-hydroxy-2-pyridinones and a dihydroxypyridine were synthesized and evaluated. The competitive inhibition constants for these first generation inhibitors are reported and interpreted in the context of X-ray crystallographic and solution X-ray absorption (EXAFS) analyses of the inhibited enzyme. The major conclusions are that the FBPA Zn²⁺ cofactor-substrate binding is weak at the ground state but strong at the transition state and that effective inhibitor design based on the use of a Zn²⁺ warhead must take into account the steric and electrostatic properties of the Zn²⁺ ligand at the transition state.

2. Materials and Methods

2.1. Determination of *GIFBPA* Inhibition Constants of 1-10

Initial velocities were measured for reactions initiated by the addition of FBP (2-20 μM) to solutions containing *GIFBPA* (0.02 μM), inhibitor (0-3K_i), 200 μM NADH, 5 units of triosephosphate isomerase, and 2 units of glycerol-3-phosphate dehydrogenase in 50 mM K⁺HEPES (pH 7.5; 25 °C). The progress of the reaction was continuously monitored at 340 nM for conversion of NADH to NAD (Δε = 6.2 mM⁻¹ cm⁻¹). The initial velocity data were fitted to eq.1.

$$V_0 = V_{\max} [S] / [K_m (1 + [I] / K_i) + [S]] \quad (1)$$

In eq. 1, [S] = substrate concentration, [I] = inhibitor concentration V₀ = initial velocity, V_{max} = maximum velocity and K_m = Michaelis-Menten constant, and K_i = the competitive inhibition constant.

2.2. Crystallization and Data Collection

The crystals of the *GIFBPA*-inhibitor **8** complex were prepared by soaking TBP-liganded crystals [25] with inhibitor **8**. The TBP-liganded crystals were grown at room temperature in hanging drops using the vapor diffusion method. The protein solution containing 10 mM TBP was mixed with an equal volume of mother liquor containing 22% polyethylene glycol 3350 and 0.2 M NH₄NO₃. The crystals required a period of 2-3 weeks to appear. Ligand exchange was accomplished by 4 rounds of transferring the crystals with a loop to a fresh solution of mother liquor containing 20 mM inhibitor **8**. The crystals diffracted X-rays to a resolution of 2.3 Å. For data collection, the crystals were transferred to solutions containing mother liquor, 20 mM inhibitor **8** and 20% glycerol, and flash-cooled in liquid nitrogen.

Diffraction data were acquired at the Southeast Regional - Collaborative Access Team (SER-CAT) 22-ID beamline at the Advanced Photon Source (APS, Argonne National Laboratory, Argonne, Illinois). For data acquisition, the SER-CAT beamline was equipped with a Quantex210 CCD detector. Data processing was carried out using CrystalClear version 1.3.6 (Rigaku MSC Inc.). The statistics of data collection are provided in Table 1.

2.3. Structure Determination and Refinement

The structure of the FBPA-inhibitor **8** complex was determined by using Molecular Replacement techniques with the computer program Phaser [26], employing the *G*/FBPA-phosphoglycolohydroxamate structure (PDB code 2ISW) as the search model rather than the *G*/FBPA-TBP structure in order to avoid phase bias. The Difference Fourier maps indicated some alternative tracing. Structure refinement was carried out using the CNS [27]. The final stages of refinement were performed with REFMAC [28]. The two molecules in the asymmetric unit were refined independently. The resulting models were inspected and modified on a graphics workstation by the using program 'O' [29]. Water molecules were added to the model based on the F_o-F_c Difference Fourier electron density map (where F_o and F_c are the observed and calculated structure factors, respectively), using peaks with density $\geq 3\sigma$ as the acceptance criteria. Refinement statistics are provided in Table 1. PROCHECK [30] was used for analysis of geometry, QUANTA for molecular modeling and structural alignment (Molecular Simulations Inc.), and PYMOL [31] for depiction of the structures.

2.4. X-ray Absorption Spectra Measurement

Buffered (50 mM K^+ HEPES, pH 7.5) *G*/FBPA (3 mM) samples were prepared with 20% (v/v) glycerol, and loaded in Lucite cuvettes with 6 μ m polypropylene windows, before rapid freezing in liquid nitrogen. *G*/FBPA activity towards catalysis of FBP cleavage was assayed (*vide supra*) in the presence of the 20% (v/v) glycerol and found to be unchanged from that observed in buffer alone. The X-ray absorption spectra were measured at the National Synchrotron Light Source (Brookhaven National Lab, Upton, NY), beamline X3B, with a Si(111) double crystal monochromator; harmonic rejection was accomplished using a Ni focusing mirror. Data collection and reduction were accomplished according to published procedures [32]. The reported spectra represent the average of the 6-8 scans per sample.

Both raw and Fourier filtered EXAFS data were fitted utilizing theoretical amplitude and phase functions calculated with FEFF v. 8.00 [33]. The Zn-N scale factor and the threshold energy, ΔE_0 , were calibrated to the experimental spectrum for tetrakis-1-methylimidazole Zn(II) perchlorate, $Zn(MeIm)_4$ and held fixed at 0.78 and -16 eV, respectively, with E_0 set to 9675 eV. First shell fits were then obtained for all reasonable coordination numbers while allowing the absorber-scatterer distance, R_{as} , and the Debye-Waller factor, σ_{as}^2 , to vary. Fits to unfiltered EXAFS, presented in the Supporting Information (Fig S11), gave identical results. In no case did inclusion of a mixed first shell, with distinct Zn-N and Zn-O scattering contributions, result in either a significant improvement in fit residual or resolvable Zn-N/Zn-O distances. Multiple scattering contributions from coordinated histidine residues were fitted using a set of combined multiple-scattering paths, according to published procedures [34].

3. Results

3.1. Inhibitor Design

The steric and electrostatic features of the *G*/FBPA substrate-binding site, defined by the structure of the *G*/FBPA-TBP complex [25] (Fig. 2A and 2B), guided the design of inhibitors (Fig. 2C). The multiple hydrogen bonds formed with the TBP C(1) and C(6) phosphate groups (Fig. 2B) suggested that the phosphate subsites supply a large fraction of the binding energy in the ground state complex ($K_i = 1 \mu$ M [25]; $\Delta G_{\text{binding}} = -8$ kcal/mol). Therefore, the inhibitor must include comparable tetrahedral dianionic substituents in order to effectively displace the substrate FBP, which also employs the phosphate groups for tight binding [13]. Because the hydrogen bonds to TBP do not involve the bridging oxygen atoms of the phosphate groups, a phosphonate group, which provides greater chemical and

metabolic stability than the phosphate ester [35], might be a useful replacement of the phosphate group.

The selection of the Zn^{2+} binding group (“ Zn^{2+} warhead”) was influenced by the demonstrated success of the hydroxypyridinone-based series of 6-membered ring Zn^{2+} chelating compounds developed by Cohen and his co-workers for targeting the Zn^{2+} center of matrix metalloproteases [36,37]. By first using the tris(pyrazoyl)borate- Zn^{2+} complex as a chemical model of the matrix metalloprotease Zn^{2+} center, these investigators showed that hydroxypyridinones displace the water ligand and engage in strong bidentate coordination with the caged Zn^{2+} to generate a 5-coordinate, trigonal bipyramidal complex (Fig. 3) [36]. Subsequently, the potencies of the hydroxypyridinone Zn^{2+} binding groups as inhibitors of the matrix metalloproteases were demonstrated, as were their metabolic stabilities and lack of toxicity [38].

In silico modeling of the 3-hydroxy-2-pyridinone to the G/FBPA active site [25] using the program AutoDock [40] indicated a good fit. Importantly, the close proximities of the ring carbonyl and hydroxyl functions with the Zn^{2+} and the Asp83, respectively, suggested the potential for strong binding interactions. The model also indicated that the attachment of the alkylphosphate/phosphonate substituents to the 3-hydroxy-2-pyridinone ring nitrogen and the *para*-carbon would place the anionic groups in the respective C(1) and C(6) phosphate-binding subsites. The structures of the first generation compounds **1-9**, prepared to test this design strategy, are given in Chart I. A close structural homolog, dihydroxypyridine **10**, was also prepared for evaluation.

3.2. Synthesis of Inhibitors 1-10

The synthetic sequences used for the preparation of the hydroxypyridinones **1-9** and the hydroxypyridine **10** are shown in Schemes 1 and 2, respectively, and the complete experimental details can be found in Appendix A. The preparation of N-phosphonomethyl-3-hydroxy-2-pyridone **1** relied on initial N-alkylation of the benzyl-protected pyridone **11** with diisopropyl bromomethylphosphonate followed by trimethylsilyl bromide promoted ester cleavage and hydrogenolysis. For preparation of 3-hydroxy-4-pyridones **2** and **6**, methoxymethyl-protected 2-chloro-3-hydroxypyridine **13** was converted to the benzyloxy analog **14**. Sequential C-4 formylation and olefination with tetraisopropyl methylene-bisphosphonate gave the 4-pyridyl vinylphosphonate diester **16**. Reduction of the alkene moiety in **16** was accompanied by hydrogenolytic cleavage of the benzyl ether to give **17**. Treatment of **17** with trimethylsilyl bromide then furnished inhibitor **2**. N-Alkylation of **17** with diisopropyl bromomethylphosphonate and ester deprotection led to inhibitor **6**. The pyridonyl ethylphosphonate **2** was prepared from intermediate **17** by treatment with trimethylsilyl bromide.

Reaction of the 4-pyridylcarboxaldehyde **15** with $NaBH_4$ served as the first step in the routes for preparation of 3-hydroxy-4-pyridones **3** and **7**. The alcohol **14**, formed in this manner, underwent O-alkylation when treated with diisopropyl bromomethylphosphonate to produce the corresponding ether **19**, which following hydrogenolytic cleavage formed **20**. Treatment of **20** with trimethylsilyl bromide afforded inhibitor **3**.

The synthetic sequence employed to prepare the N-phosphonomethyl phosphates **4** and **8** began with the protected dihydroxypyridine **14** (Scheme 1). Introduction of the C-4 hydroxyethyl group was performed by reaction of the C-4 anion of **18** with ethylene oxide. Hydrogenolytic removal of the benzyl group followed by N-phosphonomethylation gave the alcohol **29**. Transformation of **29** to the dibenzyl phosphate diester **30** was achieved by reaction with dibenzyl N,N-diisopropylphosphite followed *meta*-chloroperoxybenzoic acid oxidation. Finally, a two-step deprotection sequence was used to convert **30** to inhibitor **8**.

The phosphate analog **4** was produced from intermediate **21** by phosphorylation of the alcohol moiety and deprotection.

The route to **9R** began with Wittig olefination of aldehyde **15** to produce alkene **31**. Sharpless dihydroxylation [41] with AD-mix- β provided diol **32R** with a 95% ee. Differential protection of the hydroxyl groups in **32R** followed by hydrogenolysis generated pyridone **35R**, which was N-alkylated using dibenzyl phosphonomethyltriflate to form **36R**. Selective liberation of the terminal hydroxyl group provided alcohol **37R**, which was then converted to inhibitor **9R** by using a phosphorylation - deprotection sequence. Inhibitor **9S** was prepared by using the same route employed for **9R** except that the Sharpless AD-mix- α methodology was used to carry out dihydroxylation of **31**. The phosphate **5** was formed from intermediate **35R** by tert-butyldimethyl silyl deprotection, alcohol phosphorylation, and benzyl and methoxymethyl ether removal.

Finally, the route used for preparation of the dihydroxypyridine derivative **10** was initiated by conversion of pyridoxal (**39**) to the protected pyridine **42**. Formylation of **42** followed by sequential phosphate and phosphonate introduction gave **46**, which undergoes hydrogenolysis to form inhibitor **10**.

3.3. Kinetic Evaluation of Compounds 1-10 as GIFBPA Inhibitors

Steady-state kinetic methods were used to access the binding affinities of compounds **1-10** as inhibitors of the *G*/FBPA catalyzed conversion of FBP to DHAP and G3P at pH 7.5 and 25 °C. The initial velocity data, measured at varying FBP concentrations and changing fixed inhibitor concentrations, demonstrated that competitive inhibition was taking place in each case and yielded the inhibition constants listed in Table 2. Compounds **1-5**, which possess only one of the phosphoryl groups, were observed to bind significantly less tightly than inhibitors **7-10**, which possess two properly positioned phosphoryl groups. This finding shows that both alkylphosphate/phosphonate ring substituents (R_1 and R_2) contribute to inhibitor binding affinity. Comparisons of the inhibition constants of inhibitors **7-9** to that of inhibitor **6**, indicate that the longer R_2 linker generates more binding energy. Elaboration of inhibitor **8** by incorporation of a (*S*)-hydroxyl substituent on the R_2 linker was found to have little effect on binding as shown by the inhibition constant of inhibitor **9(S)**. However, incorporation of a (*R*)-hydroxyl substituent caused a slight impairment in binding as noted for inhibitor **9** (Table 2). Replacement of the Zn^{2+} binding group $O=C-C-OH$ in inhibitor **8** with the $HO-C-C-OH$ moiety in inhibitor **10** did not alter the value of the inhibition constant.

3.4. X-ray Crystallographic Structure Determination of GIFBPA bound with Compound 8

In order gain further insight into the structural determinants of inhibitor binding, the X-ray structure of *G*/FBPA, complexed with inhibitor **8**, was determined. The 2.3 Å resolution structure was obtained by first soaking *G*/FBPA-TBP crystals [25] with inhibitor **8** to replace the TBP ligand. The crystallization and refinement statistics are listed in Table 1, and the stereo-picture depicting of the ligand electron density is shown in Fig. 4A. As predicted by analysis of the docking model, the CH_2PO_3 group of inhibitor **8** fits nicely in the desolvated pocket where the TBP (C1)phosphate binds [25]. Likewise, the $CH_2CH_2OPO_3$ substituent of inhibitor **8** is located in the depression at the protein surface with its phosphate group bound by the residues that form the TBP C(6)phosphate binding site (Fig. 4B). Comparison of the *G*/FBPA active site binding interactions observed with inhibitor **8** (Fig. 4C) to those occurring with TBP (Fig. 2B) leads to the conclusion that inhibitor scaffold design is successful. Specifically, each of the targeted hydrogen bond donors or acceptors observed in the *G*/FBPA-TBP complex along with the Asp83, which forms a hydrogen bond to the pyridone ring OH, are observed to favorably interact with the

ligand in the *G*/FBPA-inhibitor **8** complex, although no additional binding energy is gained through incorporation of the hydroxyl substituent on the first carbon atom of the CH₂CH₂OPO₃ group (compounds **9S** and **9R**) (Table 2).

The binding of inhibitor **8** to *G*/FBPA, in analogy to substrate binding, induced the crucial conformational change that locks down the active site and places the Zn²⁺ in the proximity of the reaction center.¹ This change in Zn²⁺ coordination is depicted in Figure 5. In order to gain binding energy through interaction of the Zn²⁺ cofactor with the 3-hydroxy-2-pyridinone unit, the Zn²⁺ must form short coordination bonds (2.1 Å) with the O=C-C-OH oxygen atoms. The high B factor observed for the Zn²⁺, coupled with elongated bond distances between Zn²⁺ and the three histidine ligands (2.4-2.8 Å) and the O=C-C-OH group of compound **8** (2.7-2.9 Å), indicated that the Zn²⁺ site is not well ordered in the structure. Therefore, we interrogated the Zn²⁺ coordination state in the *G*/FBPA-inhibitor **8** complex in solution (see below).

3.5. X-ray Absorption Spectral Determination of G/FBPA Complexes

Solution X-ray absorption spectroscopy, which offers an alternative method for examining Zn²⁺ coordination in protein complexes, was used as an independent method to determine if compound **8** coordinates to the *G*/FBPA Zn²⁺. X-ray absorption spectra were obtained for the unliganded enzyme and for *G*/FBPA bound with inhibitor **8**, as well as for *G*/FBPA bound with the inhibitors phosphoglycolohydroxamate (PGH) [13] and TBP [25]. The Fourier transformed Zn K-edge EXAFS spectra are shown in Fig. 6 and curve fitting results are summarized in Table 3 and SI1; XANES spectra and fits to raw EXAFS data are presented in Supporting Information, Figures SI1 and Table SI2 (Appendix A), respectively. Although high-resolution X-ray data are not available for the unliganded *G*/FBPA, it is reasonable to assume that the 4-coordinate geometry observed for the unliganded *H. pylori* FBPA (three His ligands plus the Glu ligand) [50] is representative of that of the unliganded *G*/FBPA (Fig. 5). The XANES and EXAFS data for unliganded *G*/FBPA (Figs. 6 and SI1, Table 3) support this expectation. The best fit average bond length of 2.03 Å is wholly consistent with those determined crystallographically for four-coordinate Zn(II) complexes containing all low-Z (N/O) donors. High-resolution (1.8 Å) X-ray structures are available for the *G*/FBPA-PGH [13] and *G*/FBPA-TBP [25] complexes, and these structures clearly define a 4-coordinate Zn²⁺, consisting of three histidine ligands (H210, H178, H84) and an oxygen atom from the inhibitor ligand. The XANES spectrum, and the EXAFS-determined bond length of 2.03 Å for *G*/FBPA-TBP are nearly indistinguishable from the unliganded enzyme. The XANES and EXAFS for *G*/FBPA-PGH show some minor perturbations relative to the unliganded enzyme. However, the slight (0.04 Å) increase in first shell bond length is insufficient to suggest an increase in coordination number, although it may be indicative of slight geometric differences in the TBP and PGH complexes. The data for the *G*/FBPA-inhibitor **8** complex show minimal perturbation of the XANES and only 0.007 Å difference in average first shell bond length, which we take to indicate that Zn²⁺ in the *G*/FBPA-**8** complex coordinates to one oxygen atom of the pyridinone O=C-C-OH unit of inhibitor **8**.

¹The change in the Zn²⁺ coordination depicted in Figure 5 is based on the comparison of the structures of *H. pylori apo* FBPA (determined at 1.8 Å resolution; PDB accession code 3C4U) and the corresponding liganded structures (determined at 2.3 Å resolution; PDB accession codes 3C56 and 3C52) as well as on the comparison of the structure of *G. intestinalis apo* FBPA (determined at 2.9 Å resolution; PDB accession code 3GAK) and the TBP liganded structure (determined at 1.8 Å resolution; PDB accession code 2ISW)

4. Discussion

The EXAFS data measured for the *G*/FBPA-inhibitor **8** complex suggests that the Zn^{2+} cofactor does engage one of the pyridinone ring oxygen atoms in coordination. However, based on inspection of recent X-ray structures of liganded bacterial class II FBPA we surmise that the coordination bond will be weak. Specifically, it was reported by Fonvielle *et al.* [42] that N-(3-hydroxypropyl)-glycolohydroxamic acid bisphosphate (PGH-PrP), a hydroxamic acid analog of FBPA, binds to the *H. pylori* FBPA with high affinity ($K_i = 0.01 \mu M$) yet without the anticipated short-bond, in-plane, bidentate coordination geometry between the hydroxamic group and the Zn^{2+} cofactor. The long-range (C=O at 2.9 Å and N-OH at 2.5 Å), “out-of plane” interaction between Zn^{2+} and the hydroxamic acid group indicates that the binding energy is primarily derived from hydrogen bonding interactions between active site residues and the phosphonate and hydroxamic acid groups. PGH-PrP presents both a flexible, substrate-like scaffold and a powerful Zn^{2+} binding group. The absence of tight, bidentate Zn^{2+} coordination in this complex is striking, but can be rationalized in light of the respective structures of the *Mycobacterium tuberculosis* FBPA bound with FBPA or the charged enediolate form of DHAP reported by Mesecar and coworkers [43]. Whereas the Zn^{2+} is observed to be centered above the plane of FBPA O=C(2)-C(3)(OH)-C(4)OH moiety and thus not engaged in strong coordination to any one of the three potential oxygen ligands, the DHAP enediolate participates in strong, in-plane bidentate coordination of Zn^{2+} (C(1)O at 2.1 Å and C(2)O at 2.2 Å). The DHAP enediolate is the reaction intermediate formed by the C(3)-C(4) cleavage step of FBPA catalysis (Fig. 1).

Taken together, the structures of FBPA bound with substrate (FBP) or substrate mimics (TBA, PGH-PrP and inhibitor **8**) provide solid evidence that the Zn^{2+} cofactor does not engage the substrate in strong coordination bonding and, thus, it does not significantly contribute to the substrate binding energy. The structure of FBPA bound with the DHAP enediolate is definitive proof that the Zn^{2+} cofactor engages in strong coordination bonding as the substrate changes to product along the reaction coordinate. The ability of a Zn^{2+} cofactor to modify its coordination with the reactant as it is transformed along the enzyme catalyzed reaction coordinate is well documented [44].

5. Conclusions

In conclusion, we propose that the *G*/FBPA Zn^{2+} cofactor functions in transition state/intermediate stabilization and not in the stabilization of the enzyme-substrate complex. Substrate binding induces a conformational change that dissociates the Glu135 ligand as the Zn^{2+} moves to the reaction center (Fig. 5). This induced-fit mechanism presents a challenge to inhibitor design strategies, which rely on recruiting the binding energy associated with Zn^{2+} coordination because substrate binding is used to drive the required conformational change rather than engage the Zn^{2+} in strong coordination. Consequently, for optimal binding a *G*/FBPA inhibitor should include a phosphonate substituent to fill the C(1)phosphate binding site (Fig. 2) and induce the conformational change, while at the same time containing a negatively charged substituent, such as a thiolate, to form a strong coordination bond to the Zn^{2+} cofactor.

Supplementary Material

Refer to Web version on PubMed Central for supplementary material.

Acknowledgments

This work was supported by NIH grant AI059733 to O. H., D.D.-M. and P. S. M and by NSF CHE-0964806 grant to D. L.T.

References

1. Adam RD. Biology of *Giardia lamblia*. *Clin Microbiol Rev.* 2001; 14:447–475. [PubMed: 11432808]
2. Barwick RS, Levy DA, Craun GF, Beach MJ, Calderon RL. *MMWR CDC Surveill Summ.* 2000; 49:1. [PubMed: 10843502]
3. Farthing MJ. Giardiasis. *Gastroenterol Clin North Am.* 1996; 25:493–515. [PubMed: 8863037]
4. WHO (World Health Organization). 1998 World Health Report: Life in the 21st century: A vision for all. Geneva: World Health Organization; 1998.
5. Boreham PF, Phillips RE, Shepherd RW. *Trans R Soc Trop Med Hyg.* 1988; 82:104–106. [PubMed: 3176140]
6. Zaat JO, Mank TG, Assendelft WJ. *Trop Med Int Health.* 1997; 2:63–82. [PubMed: 9018304]
7. Upcroft P, Upcroft JA. *Clin Microbiol Rev.* 2001; 14:150–164. [PubMed: 11148007]
8. Wright JM, Dunn LA, Upcroftand P, Upcroft JA. *Expert Opin Drug Saf.* 2003; 2:529–541. [PubMed: 14585063]
9. McArthur AG, Morrison HG, Nixon JE, Passamaneck NQ, Kim U, Hinkle G, Crocker MK, Holder ME, Farr R, Reich CI, Olsen GE, Aley SB, Adam RD, Gillin FD, Sogin ML. *FEMS Microbiol Lett.* 2000; 189:271–273. [PubMed: 10930750]
10. Jarroll EL, Manning P, Berrada A, Hare D, Lindmark DG. *J Protozool.* 1989; 36:190–197. [PubMed: 2657035]
11. Lindmark DG. *Giardia lamblia*. *Mol Biochem Parasitol.* 1980; 1:1–12. [PubMed: 6108507]
12. Muller M. *Annu Rev Microbiol.* 1988; 42:465–488. [PubMed: 3059999]
13. Galkin A, Kulakova L, Melamud E, Li L, Wu C, Mariano PS, Dunaway-Mariano D, Nash TE, Herzberg OJ. *Biol Chem.* 2007; 282:4859.
14. Henze K, Morrison HG, Sogin ML, Muller M. *Giardia lamblia*. *Gene.* 1998; 222:163–168.
15. Rutter WJ. *Fed Proc.* 1964; 23:1248–1257. [PubMed: 14236133]
16. Kobes RD, Simpson RT, Vallee RI, Rutter WJ. *Biochemistry.* 1969; 8:585–588. [PubMed: 5793710]
17. Belasco JG, Knowles JR. *Biochemistry.* 1983; 22:122–129. [PubMed: 6338912]
18. Kadonaga JT, Knowles JR. *Biochemistry.* 1983; 22:130–136. [PubMed: 6338913]
19. Grazi E, Cheng T, Horecker BL. *Biochem Biophys Res Commun.* 1962; 7:250–253. [PubMed: 13901342]
20. Horeker BL, Rowley PT, Grazi E, Cheng T, Tchola O. *Biochem Z.* 1963; 338:36–51. [PubMed: 14087308]
21. Model P, Ponticorvo L, Rittenberg D. *Biochemistry.* 1968:1339–1347. [PubMed: 5677823]
22. Supuran CT. *Curr Pharm Design.* 2008; 14:603–614.
23. Hong X, Hammell M, Ambros V, Cohen SM. *Biochim Biophys Acta.* 2010; 1803:72–94. [PubMed: 19712708]
24. Acharya MR, Sparreboom A, Venitz J, Figg WD. *Mol Pharmacol.* 2005; 68:917–32. [PubMed: 15955865]
25. Galkin A, Li Z, Li L, Kulakova L, Pal LR, Dunaway-Mariano D, Herzberg OJ. *Biochemistry.* 2009; 48:186–96.
26. McCoy AJ, Grosse-Kunstleve RW, Storoni LC, Read RJ. *Acta Cryst.* 2005; D60:432–438.
27. Brunger AT, Adams PD, Clore GM, DeLano WL, Gros P, Grosse-Kunstleve RW, Jiang JS, Kuszewski J, dNilges M, Pannu NS, Read RJ, Rice LM, Simonson T, Warren GL. *Acta Cryst.* 1998; D54:905–921.
28. Winn MD, Isupov MN, Murshudov GN. *Acta Cryst.* 2001; D57:122–133.

29. Jones TA. Acta Cryst. 2004; D60:2115–2125.
30. Laskowski RA, MacArthur MW. J Appl Crystallogr. 1993; 26:283–291.
31. DeLano, WL. The PyMOL User's Manual. DeLano Scientific; San Carlos, CA, USA: 2002.
32. Thomas PW, Stone EM, Costello AL, Tierney DL. Biochemistry. 2005; 44:7559–7569. [PubMed: 15895999]
33. Ankudinov AL, Ravel B, Rehr JJ, Conradson SD. Phys Rev B. 1998; 58:7565–7576.
34. Costello AL, Periyannan G, Yang KW, Crowder MW, Tierney DL. J Biol Inorg Chem. 2006; 11:351–358. [PubMed: 16489411]
35. Dang Q. Expert Opin Ther Patents. 2006; 16:343–348.
36. Puerata DT, Cohen SM. Inorg Chem. 2003; 42:3423–3430. [PubMed: 12767177]
37. Puerata DT, Lewis JA, Cohen SM. J Amer Chem Soc. 2004; 126:8388–8389. [PubMed: 15237990]
38. Puerata DT, Griffen MO, Lewis JA, Romero-Perez D, Garcia R, Villarreal FJ, Cohen SM. J Biol Inorg Chem. 2006; 11:131–138. [PubMed: 16391944]
39. Pegan SD, Ruckseree KM, Franzblau SG, Mesecar AD. J Mol Biol. 2009; 386:1038–1053. [PubMed: 19167403]
40. Morris GM, Goodsell DS, Halliday rS, Huey R, Hart WE, Belew RK, Olson JA. J Comp Chem. 1998; 19:1639–1662.
41. Kolb HC, VanNieuwenhze M, Sharpless KB. Chem Rev. 1994; 94:2483.
42. Fonvielle M, Coinçon M, Daher R, Desbenoit N, Kosieradzka K, Barilone N, Gicquel B, Sygusch J, Jackson M, Therisod M. Chem Eur J. 2008; 14:8521–8529.
43. Pegan SD, Rukseree K, Franzblau SG, Mesecar AD. J Mol Biol. 2009; 386:1038–1053. [PubMed: 19167403]
44. Baker PJ, Britton KL, Fisher M, Esclapez j, Pire C, Bonete MJ, Ferrer J, Rice D. Proc Nat Acad Sci U S A. 2009; 106:779–784.

Abbreviations

FBP	Fructose 1,6 bisphosphate
FBPA	fructose 1,6 bisphosphate aldolase
G/FBPA	<i>Giardia lamblia</i> fructose 1,6 bisphosphate aldolase
TBP	tagatose 1,6 bisphosphate
G3P	glyceraldehyde 3-phosphate
DHAP	dihydroxyacetone phosphate
HEPES	4-(2-hydroxyethyl)-1-piperazineethanesulfonic acid
EXAFS	extended X-ray absorption fine structure
EXAFS	extended x-ray absorption spectroscopy

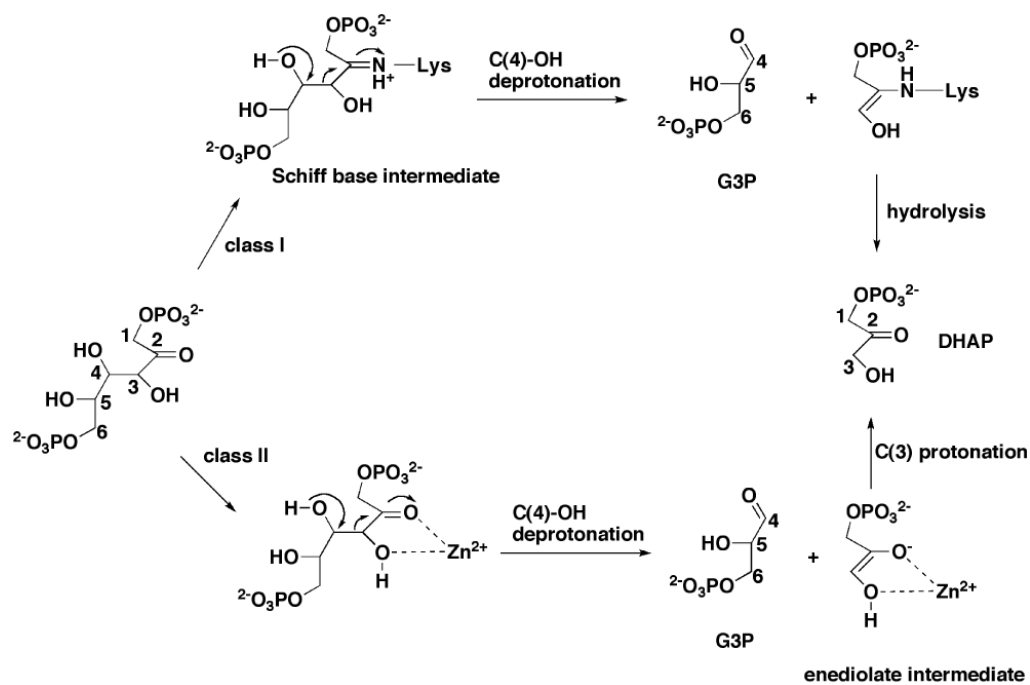


Figure 1.
The reaction pathways catalyzed by class I and class II fructose 1,6-bisphosphate aldolases.

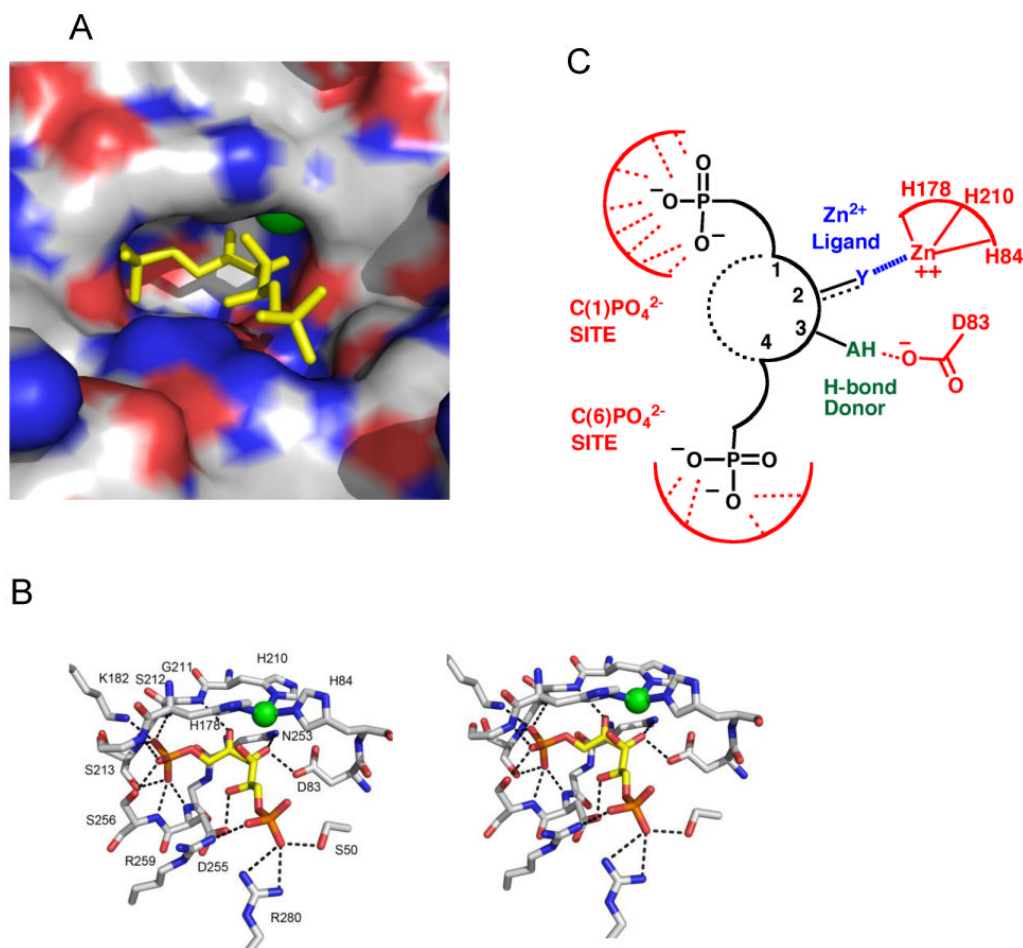


Figure 2. **A.** Surface representation of the substrate-binding site observed in the structure of the *G/FBPA-TBP* complex (PDB: 3GAY). The enzyme nitrogen atoms are colored, carbons atoms white and oxygen atoms red. The Zn^{2+} cofactor is shown as a green sphere and the TBP ligand as yellow sticks. **B.** The stereoview of the *G/FBPA-TBP* complex (PDB: 3GAY) substrate-binding site. Hydrogen bonds are represented with black dashed lines. The carbon atoms of the TBP are colored yellow, oxygen atoms red and phosphorus atoms orange. **C.** Cartoon representation of the inhibitor design.

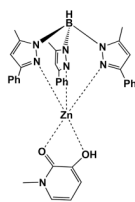


Figure 3.
Chemdraw representation of the 5-coordinate, trigonal bipyramidal complex
tris(pyrazoyl)borate-Zn²⁺-hydroxypyridinone complex adopted from reference [43].

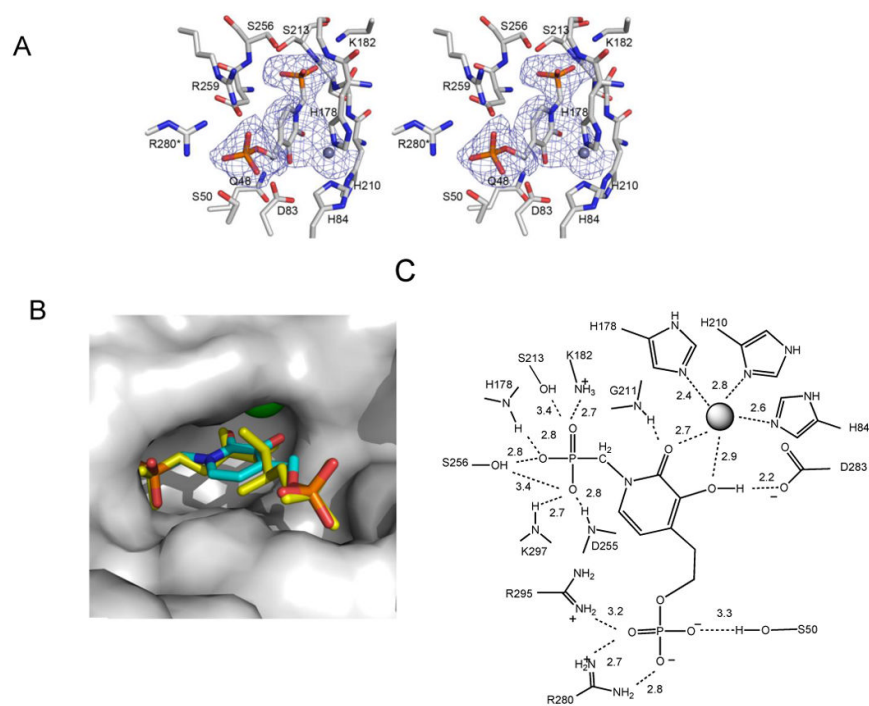


Figure 4.

A. Stereoviews of the *G/FBPA*-inhibitor **8** complex electron density map showing the electron density of inhibitor **8** and the Zn^{2+} cofactor. **B.** Superposition of the structures of the *G/FBPA*-TBP and *G/FBPA*-inhibitor **8** complexes. The FBP is colored yellow and the inhibitor **8** is colored cyan (carbon), red (oxygen) and orange (phosphorus). The surface of the *G/FBPA*-inhibitor **8** complex is shown in gray. **C.** Chemdraw representation of the nonbonding interactions observed for inhibitor **8** in the *G/FBPA*-inhibitor **8** complex. The distances are provided in Å.

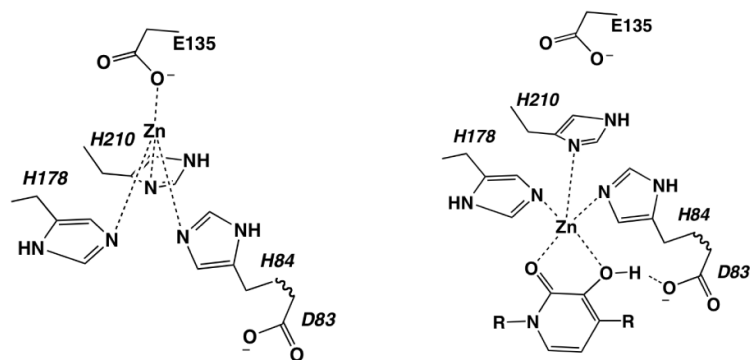


Figure 5. Chemdraw representation of the anticipated change in the *G/FBPA* Zn²⁺ coordination state upon inhibitor **8** association.

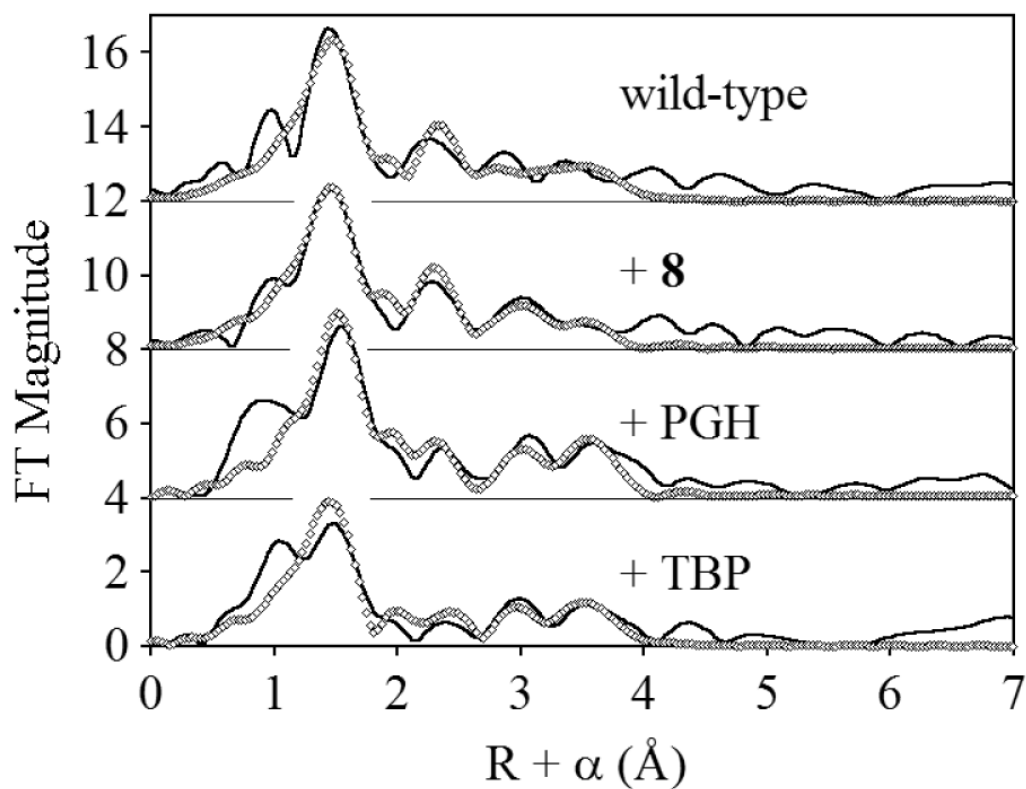
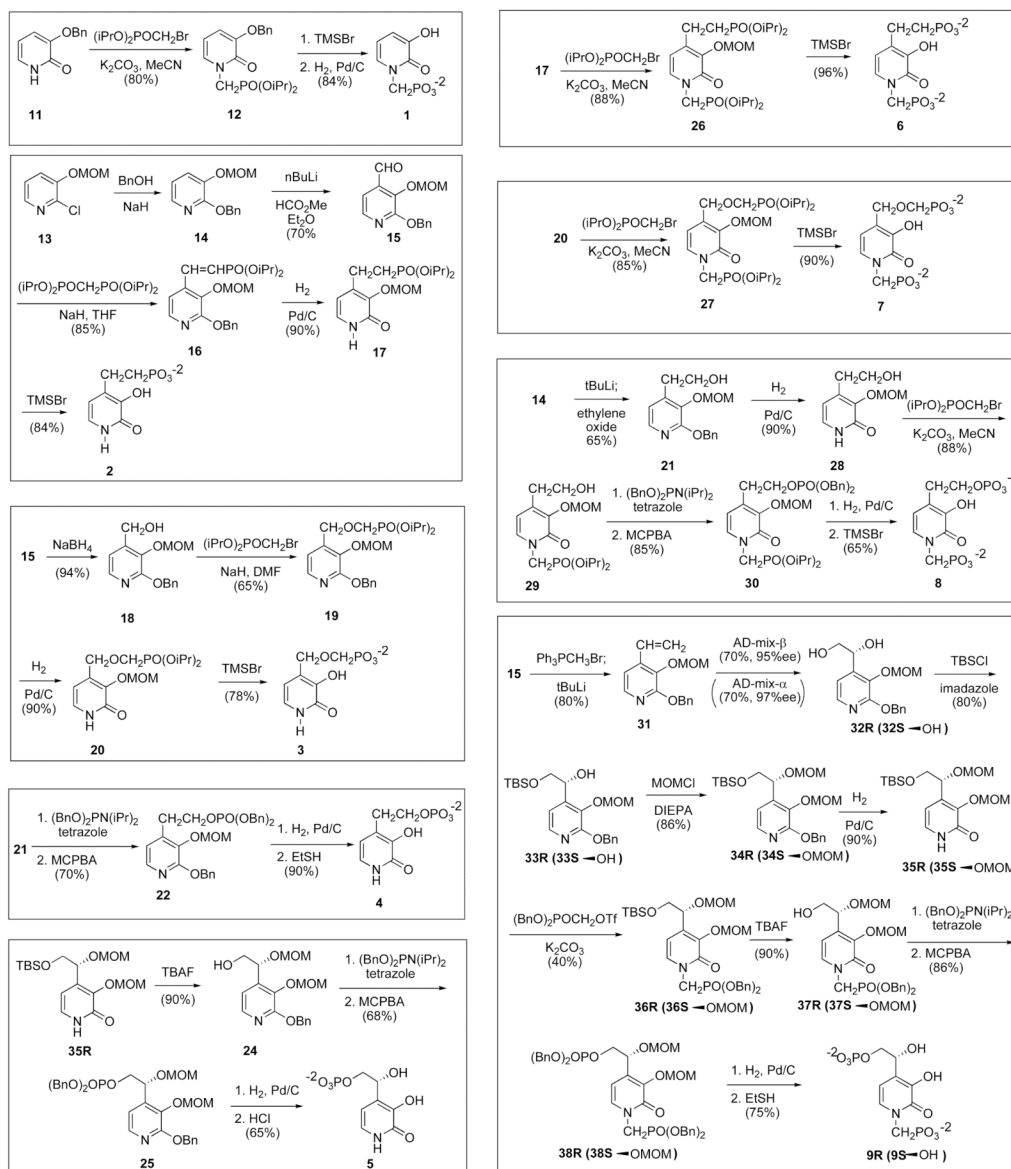
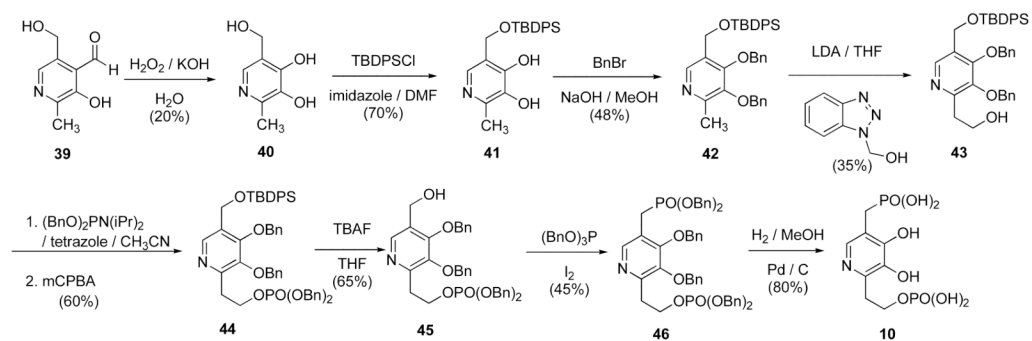


Figure 6. Fourier transformed Zn K-edge EXAFS (solid lines) and corresponding best fits (open symbols, see Table 0) measured for unliganded *G/IFBPA* (labeled “wild-type”) and *G/IFBPA* complexes of inhibitor 8, PGH and TBP. See Experimental for details.

**Scheme 1.**The reaction sequences used in the syntheses of inhibitors **1-9**.

**Scheme 2.**

The reaction sequence used in the synthesis of inhibitor **10**.

Table 1X-ray data collection and refinement statistics for the *GIFBPA*-inhibitor **8** complex.

Data collection	
Space group	P2 ₁ 2 ₁ 2 ₁
Cell dimension a, b, c (Å)	58.58, 64.95, 171.45
Resolution range (Å)	20.0-2.3
No. observations	108611
No. unique reflections	23705
Completeness (%) ^a	86.5(89.1)
R_{merge} ^b	0.079(0.248)
Refinement statistics	
No. reflections	22497
No. residues	635
No. water molecules	339
R_{work} ^c	0.199
R_{free} ^d	0.274
RMS deviation	Bonds (Å) 0.014; Angles (°) 1.5

^aThe values in parentheses are for the highest resolution shell^b $R_{merge} = \sum_{hkl} [(\sum_j |I_j - \langle I \rangle|) / \sum_j |I_j|]$, for equivalent reflections^c $R_{work} = \sum_{hkl} ||F_o| - |F_c|| / \sum_{hkl} |F_o|$, where F_o and F_c are the observed and calculated structure factors included in the refinement, respectively^d R_{free} is computed for 5% of reflections that were randomly selected and omitted from the refinement

Table 2

G/FBPA inhibition constants (K_i) measured for compounds **1-10** vs FBP at pH 7.5 and 25 °C (see Experimental for details).

Compound	K_i (μM)	Compound	K_i (μM)
1	1200 \pm 200	7	110 \pm 10
2	810 \pm 50	8	14 \pm 4
3	970 \pm 50	9R	90 \pm 6
4	900 \pm 200	9S	10 \pm 2
5	2300 \pm 500	10	15 \pm 2
6	800 \pm 100	TBP	1

Table 3
Best fits to EXAFS data measured for *apo* G/FBPA and G/FBPA-ligand complexes.^a

Model	Zn-N/O	Zn-His ^b	R _f ^c	R _u ^c
<i>apo</i> G/FBPA	4 @ 2.030 (6.7)	2.91 (3.4)	3.17 (3.8) 4.22 (14)	4.41 (16) 106 448
G/FBPA-8	4 @ 2.023 (6.4)	2.92 (2.6)	3.19 (1.7) 4.20 (24)	4.42 (19) 77 357
G/FBPA-PGH	4 @ 2.068 (4.6)	2.92 (5.4)	3.20 (2.1) 4.18 (8.3)	4.40 (18) 78 366
G/FBPA-TBP	4 @ 2.031 (8.5)	2.95 (10)	3.17 (2.9) 4.20 (11)	4.40 (16) 102 467

^aDistances (Å) and disorder parameters (in parentheses, σ^2 (10^{-3} Å²)) shown derive from integer coordination number fits to filtered EXAFS data [$\Delta k = 1-11$ Å⁻¹; $\Delta R = 0.3-4.0$ Å]

^bMultiple scattering paths represent combined paths, as described previously (see Materials and Methods)

^cGoodness of fit (R_f for fits to filtered data; R_u for fits to raw data) defined as

$$1000 * \frac{\sum_{i=1}^N \{ [\text{Re}(\chi_{\text{calc}})]^2 + [\text{Im}(\chi_{\text{calc}})]^2 \}}{\sum_{i=1}^N \{ [\text{Re}(\chi_{\text{obs}})]^2 + [\text{Im}(\chi_{\text{obs}})]^2 \}},$$

where N is the number of data points.